Micropipe flow visualization using digital in-line holographic microscopy

Nicolas Verrier, Clément Remacha, Marc Brunel, Denis Lebrun, Sébastien Coëtmellec

Micropipe flow visualization using digital in-line holographic microscopy

Nicolas Verrier,[1,*] Clément Remacha[1], Marc Brunel[1], Denis Lebrun[1], and Sébastien Coëtmellec[1,2]

[1]*Groupe d'Optique et d'Optoélectronique, UMR 6614-CORIA, avenue de l'Université, 76801 Saint-Etienne du Rouvray cédex, France*
[2]*sebastien.coetmellec@coria.fr*
**nicolas.verrier@coria.fr*

Abstract: Digital in-line holography is used to visualize particle motion within a cylindrical micropipe. Analytical expression of the intensity distribution recorded in the CCD sensor plane is derived using the generalized Huygens-Fresnel integral associated with the ABCD matrices formalism. Holograms obtained in a 100µm in diameter micropipe are then reconstructed using fractional Fourier transformation. Astigmatism brought by the cylindrical micropipe is finally used to select a three dimensional region of interest in the microflow and thus to improve axial localization of objects located within a micropipe. Experimental results are presented and a short movie showing particle motion within a micropipe is given.

OCIS codes: (090.0090) Holography; (070.0070) Fourier optics and signal processing;

References and Links

1. M. Malek, D. Allano, S. Coëtmellec, C. Özkul, and D. Lebrun, "Digital in-line holography for three-dimensional-two-components particle tracking velocimetry," Meas. Sci. Technol. **15**(4), 699–705 (2004).
2. E. Malkiel, J. Sheng, J. Katz, and J. R. Strickler, "The three-dimensional flow field generated by a feeding calanoid copepod measured using digital holography," J. Exp. Biol. **206**(20), 3657–3666 (2003).
3. W. Xu, M. H. Jericho, I. A. Meinertzhagen, and H. J. Kreuzer, "Digital in-line holography for biological applications," Proc. Natl. Acad. Sci. U.S.A. **98**(20), 11301–11305 (2001).
4. J. Garcia-Sucerquia, W. Xu, S. K. Jericho, P. Klages, M. H. Jericho, and H. J. Kreuzer, "Digital in-line holographic microscopy," Appl. Opt. **45**(5), 836–850 (2006).
5. J. Garcia-Sucerquia, W. Xu, M. H. Jericho, and H. J. Kreuzer, "Immersion digital in-line holographic microscopy," Opt. Lett. **31**(9), 1211–1213 (2006).
6. W. Xu, M. H. Jericho, H. J. Kreuzer, and I. A. Meinertzhagen, "Tracking particles in four dimensions with in-line holographic microscopy," Opt. Lett. **28**(3), 164–166 (2003).
7. J. Darabi, M. M. Ohabi, and D. Devoe, "An electrohydrodynamic polarization micropump for electronic cooling," J. Microelectromech. Syst. **10**(1), 98–106 (2001).
8. C. D. Meinhart, and H. Zhang, "The flow structure inside a microfabricated inkjet printhead," J. Microelectromech. Syst. **9**(1), 67–75 (2000).
9. D. Sinton, "Microscale flow visualization," Microfluid. Nanofluid. **1**(1), 2–21 (2004).
10. C. S. Vikram, "Particle Field Holography" in *Cambridge Studies in Modern optics* (Cambridge U. Press, 1992).
11. S. Satake, T. Kunugi, K. Sato, and T. Ito, "Digital holographic particle tracking velocimetry for 3-D transient flow around an obstacle in a narrow channel," Opt. Rev. **11**, 162–164 (2004).
12. S. Satake, T. Kunugi, K. Sato, T. Ito, and J. Taniguchi, "Three-dimensional flow tracking in a micro-channel with high time resolution using micro digital-holographic particle-tracking velocimetry," Opt. Rev. **12**(6), 442–444 (2005).
13. S. Satake, T. Kunugi, K. Sato, T. Ito, H. Kanamori, and J. Taniguchi, "Measurements of 3D flow in a micro-pipe via micro digital holographic particle tracking velocimetry," Meas. Sci. Technol. **17**(7), 1647–1651 (2006).
14. S. Satake, H. Kanamori, T. Kunugi, K. Sato, T. Ito, and K. Yamamoto, "Parallel computing of a digital hologram and particle searching for microdigital-holographic particle-tracking velocimetry," Appl. Opt. **46**(4), 538–543 (2007).
15. S. Satake, T. Anraku, H. Kanamori, T. Kunugi, K. Sato, and T. Ito, "Measurement of three-dimensional flow in microchannel with complex shape by micro-digital-holographic particle-tracking velocimetry," J. Heat Transfer **130**(4), 042413 (2008).
16. N. Verrier, S. Coëtmellec, M. Brunel, and D. Lebrun, "Digital in-line holography in thick optical systems: application to visualization in pipes," Appl. Opt. **47**(22), 4147–4157 (2008).
17. S. A. Collins, Jr., "Lens-system diffraction integral written in terms of matrix optics," J. Opt. Soc. Am. **60**(9), 1168–1177 (1970).

#123897 - $15.00 USD Received 5 Feb 2010; revised 19 Mar 2010; accepted 22 Mar 2010; published 30 Mar 2010

18. F. Nicolas, S. Coëtmellec, M. Brunel, D. Allano, D. Lebrun, and A. J. E. M. Janssen, "Application of the fractional Fourier transformation to digital holography recorded by an elliptical, astigmatic Gaussian beam," J. Opt. Soc. Am. A **22**(11), 2569–2577 (2005).
19. N. Verrier, S. Coëtmellec, M. Brunel, D. Lebrun, and A. J. E. M. Janssen, "Digital in-line holography with an elliptical, astigmatic Gaussian beam: wide-angle reconstruction," J. Opt. Soc. Am. A **25**(6), 1459–1466 (2008).
20. N. Verrier, S. Coëtmellec, M. Brunel, and D. Lebrun, "Determination of 3D-region of interest using digital in-line holography with astigmatic Gaussian beams," J. Europ. Opt. Soc. Rap. Public **4**, 09038 (2009).
21. U. Schnars, and W. Jüptner, "Direct recording of holograms by a CCD target and numerical reconstruction," Appl. Opt. **33**(2), 179–181 (1994).
22. C. Palma, and V. Bagini, "Extension of the Fresnel transform to ABCD systems," J. Opt. Soc. Am. A **14**(8), 1774–1779 (1997).
23. H. T. Yura, and S. G. Hanson, "Optical beam wave propagation through complex optical systems," J. Opt. Soc. Am. A **4**(10), 1931–1948 (1987).
24. J. J. Wen, and M. Breazeale, "A diffraction beam expressed as the superposition of Gaussian beams," J. Acoust. Soc. Am. **83**(5), 1752–1756 (1988).
25. X. Du, and D. Zhao, "Propagation of decentered elliptical Gaussian beams in apertured and nonsymmetrical optical systems," J. Opt. Soc. Am. A **23**(3), 625–631 (2006).
26. X. Du, and D. Zhao, "Propagation of elliptical Gaussian beams in apertured and misaligned optical systems," J. Opt. Soc. Am. A **23**(8), 1946–1950 (2006).
27. H. M. Ozaktas, Z. Zalevsky, and M. A. Kutay, *The Fractional Fourier Transform: with Application in Optics and Signal Processing* (Wiley, 2001).
28. V. Namias, "The fractional order Fourier transform and its application to quantum mechanics," J. Inst. Math. Appl. **25**(3), 241–265 (1980).
29. A. C. McBride, and F. H. Kerr, "On Namias's fractional Fourier transforms," IMA J. Appl. Math. **39**(2), 159–175 (1987).
30. A. W. Lohmann, "Image rotation, Wigner rotation, and the fractional Fourier transform," J. Opt. Soc. Am. A **10**(10), 2181–2186 (1993).
31. P. Pellat-Finet, "Fresnel diffraction and the fractional-order Fourier transform," Opt. Lett. **19**(18), 1388–1390 (1994).

1. Introduction

Digital holography is a recognized technique for flow characterization. As a matter of fact, domains such as fluid mechanics or biological imaging benefit from the three dimensional information contained by one hologram [1–3]. Microscale extension of digital holography makes it possible to visualize and track particle as small as a few micrometers [4–6]. Digital holography is therefore a good candidate for microfluidics studies. Microfluidics aims to manipulate small amounts of liquid within microchannels with dimensions of few hundreds micrometers, and find many applications in electronic component cooling [7] or document printing [8]. Imaging through these channels is a challenging problem [9]. In fact, due to their cylindrical geometry, microchannels introduce aberrations such as astigmatism in the imaging system [10]. These unwanted effects make it difficult to retrieve information about seeding particles located in the channel. In order to overcome these limitations, Satake *et al.* used microfabricated channels, coated with water, and with a refractive index almost equal to that of water. Thus doing, the authors succeeded in obtaining three-dimensional velocity fields in various types of microfluidics devices without astigmatism [11–15].

Recently, an analytical solution of the scalar diffraction, produced by an elliptical object, located in a thick transparent pipe has been proposed [16]. Using the generalized Huygens-Fresnel transformation associated with the ABCD transfer matrix formalism [17], the authors managed to simulate holograms of elliptical objects in thick pipe with a good accordance between experimental and numerical data. Hologram reconstruction is hereby performed using fractional Fourier transformation (FRFT). As a matter of fact, it has been shown that this method is well suited when flows are studied under astigmatic illumination [18,19]. FRFT reconstruction makes it possible for the authors of Ref [16]. to visualize seeding particles in a pipe flow without astigmatism.

Here, we aim to apply digital in-line holography to visualize 5µm in diameter latex beads through a 100µm in internal diameter and 4 mm in external diameter cylindrical microchannel. In the first part of the paper, calculations leading to the intensity distribution of the diffracted field produced by an opaque object are recalled. In the second part, the mathematical expression of the FRFT is recalled and optimal fractional order values are derived according to the experimental set-up. Both numerical and experimental results are

#123897 - $15.00 USD Received 5 Feb 2010; revised 19 Mar 2010; accepted 22 Mar 2010; published 30 Mar 2010

proposed. Then, by modifying the experimental set-up, we show that, using the experimental method proposed in Ref [20], a three-dimensional region of interest (ROI) can be selected and studied in a micropipe flow. Finally, by modifying the CCD sensor to pipe distance, we prove the ability of our method to enhance particle axial localization.

2. In-line holography through a cylindrical microchannel

2.1. Simulation of the recorded intensity distribution

In digital holographic imaging, interferences between the reference beam (part of the beam that passes through the studied volume without being disturbed by the seeding particles) and the part of the beam which is diffracted by the objects are recorded on a CCD sensor without objective lens [21]. The experimental set-up used to visualize particles through a microchannel is given in Fig. 1. The beam coming from a fiber coupled laser diode propagates over a distance z_p to a microscope objective with a numerical aperture ("ON" on Fig. 1) of 0.45. The microscope objective is located at a distance z_{l_1} from the microchannel and is used to focalize the beam into the studied volume. The diffracting object is located at a distance δ from the microchannel inlet. The CCD sensor used to record the holograms is positioned at a distance z from the micropipe.

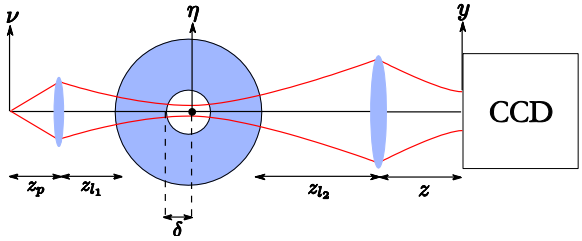

Fig. 1. Experimental and recording set-up of digital in-line holograms

Propagation of a Gaussian point-source, denoted G, through the set-up presented Fig. 1, is considered. The amplitude distribution of the point-source is given by:

$$G(\mu,\nu)=\exp\left(-\frac{\mu^2+\nu^2}{\omega^2}\right), \tag{1}$$

where, ω is the waist radius and (μ,ν) the coordinates in the fiber coupled laser diode plane. Propagation of G from the pinhole to the CCD sensor plane can be divided into two steps. First of all, propagation of $G(\mu,\nu)$ from the pinhole to the particle plane is considered. Then, interferences between the reference and the diffracted beam are calculated in the CCD sensor plane. The recorded intensity distribution is given by:

$$I(x,y)=\frac{1}{\lambda^2 B_2^x B_2^y}\left(|\mathcal{R}|^2-2\Re\left\{\mathcal{R}\overline{\mathcal{O}}\right\}+|\mathcal{O}|^2\right), \tag{2}$$

where, $\mathcal{R}$ corresponds to the reference beam, and $\mathcal{O}$ is associated with the beam diffracted by the object located in the microchannel. Mathematical expressions of the reference and the diffracted beams are derived, under paraxial conditions, using the generalized Huygens-Fresnel integral [22,23]. The reference beam is therefore given by:

#123897 - $15.00 USD Received 5 Feb 2010; revised 19 Mar 2010; accepted 22 Mar 2010; published 30 Mar 2010

$$\mathcal{R}(x,y)=\int_{\mathbb{R}^2} G_1(\xi,\eta)\exp\left[i\frac{\pi}{\lambda B_2^x}\left(A_2^x\xi^2-2x\xi+D_2^x x^2\right)\right]\times\exp\left[i\frac{\pi}{\lambda B_2^y}\left(A_2^y\eta^2-2y\eta+D_2^y y^2\right)\right]d\xi d\eta. \tag{3}$$

Here, $G_1(\xi,\eta)$ is the beam amplitude distribution in the particle plane. Coefficients $A_2^{x,y}$, $B_2^{x,y}$, and $D_2^{x,y}$ are the elements of the ABCD matrix used to characterize propagation between the particle and the CCD plane. Further explanations about determination of these coefficients can be found in Ref [16]. After analytical developments, the amplitude distribution of the reference beam is (see Appendix for further details):

$$\mathcal{R}(x,y)\propto\exp\left[-\frac{\pi}{\lambda}\left(\frac{N_x}{B_2^x}x^2+\frac{N_y}{B_2^y}y^2\right)\right]\exp\left[i\frac{\pi}{\lambda}\left(\frac{M_x}{B_2^x}x^2+\frac{M_y}{B_2^y}y^2\right)\right]. \tag{4}$$

Here, parameters $M_{x,y}$ and $N_{x,y}$ both contain information about the beam width and the wavefront curvature in the CCD sensor plane.

Amplitude distribution of the diffracted beam can be determined using the following generalized Huygens-Fresnel integral:

$$\mathcal{O}(x,y)=\int_{\mathbb{R}^2} G_1(\xi,\eta)T(\xi,\eta)\exp\left[i\frac{\pi}{\lambda B_2^x}\left(A_2^x\xi^2-2x\xi+D_2^x x^2\right)\right]\times\exp\left[i\frac{\pi}{\lambda B_2^y}\left(A_2^y\eta^2-2y\eta+D_2^y y^2\right)\right]d\xi d\eta, \tag{5}$$

where, $T(\xi,\eta)$ is the transmission function of an ellipsoidal particle. By assuming that latex beads can be considered as opaque particles, its mathematical expression is [24–26]:

$$T(\xi,\eta)=\sum_{k=1}^{N}A_k\exp\left[-\frac{B_k}{b^2}\left(\xi^2+R_{ell}^2\eta^2\right)\right] \tag{6}$$

where b is the particle width and R_{ell} stands for the ellipticity ratio of the considered particle. To simulate our opaque objects, N is fixed to 10. Values of A_k and B_k are determined by numerical resolution of Kirchhoff equation [24]. Let R_{ell} be the particle ellipticity ratio. Considering $R_{ell}=1$ leads to the simulation of a circular particle and $R_{ell}\neq 1$ is used to simulate elliptical objects. The limit case where, $R_{ell}\to 0$, is associated with an opaque fiber perpendicular to the optical axis of the system. By introducing Eq. (6) in Eq. (5), theoretical expression of the amplitude distribution of the diffracted beam becomes:

$$\mathcal{O}(x,y)\propto\exp\left[i\frac{\pi}{\lambda}\left(\frac{D_2^x}{B_2^x}x^2+\frac{D_2^y}{B_2^y}y^2\right)\right]\sum_{k=1}^{N}A_k K_2^{x_{eq}}K_2^{y_{eq}}\times\exp\left[-\frac{\pi}{\lambda}\left(\frac{N_{x_{eq}}}{B_2^x}x^2+\frac{N_{y_{eq}}}{B_2^y}y^2\right)\right]\exp\left[i\frac{\pi}{\lambda}\left(\frac{M_{x_{eq}}}{B_2^x}x^2+\frac{M_{y_{eq}}}{B_2^y}y^2\right)\right], \tag{7}$$

where $M_{x,y_{eq}}$ and $N_{x,y_{eq}}$ are respectively used to determine the width and the wavefront curvature of the diffracted beam.

#123897 - $15.00 USD Received 5 Feb 2010; revised 19 Mar 2010; accepted 22 Mar 2010; published 30 Mar 2010

2.2. Qualitative validation of the simulations

In section 2.1, analytical developments have been proposed under paraxial conditions. In order to evaluate the abilities of the presented approach to deal with micropipe flow holograms, comparison between experimental and simulation data has to be performed. The experimental set-up proposed in Fig. 1 is considered. Here, the laser source consists in a $10mW$ fiber coupled laser diode of wavelength $\lambda = 635nm$. Holograms are recorded on a 1280×1024 CMOS sensor with a pixel pitch of $6.7\mu m$. A close-up view of the micropipe used is shown in Fig. 2.

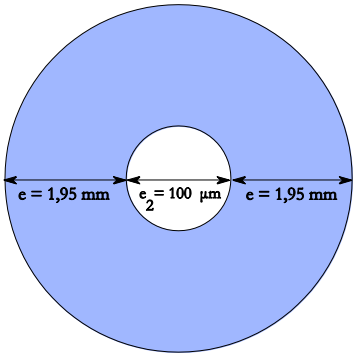

Fig. 2. Close-up (not to scale) of the micropipe used

The considered micropipe is $4mm$ in external diameter and $100\mu m$ in internal diameter. It is made of glass (refractive index $n_1 \approx 1.5$) and filled in with water (refractive index $n_2 \approx 1.33$). In order to record holograms, $5\mu m$ in diameter latex beads are injected into the microchannel.

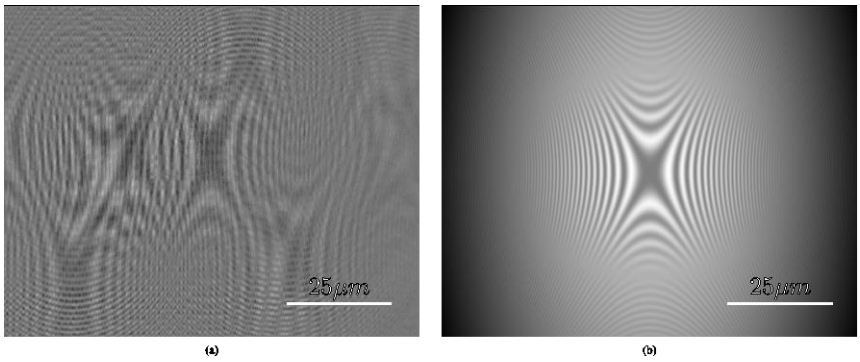

Fig. 3. Holograms obtained with $z_p = 13mm$ and $z_{l_1} = 1mm$. (a) Experimental hologram. (b) Simulated hologram.

The distance between the laser source and the x20 microscope objective is fixed to $z_p = 13mm$. The latter is located at a distance $z_{l_1} = 1mm$ from the micropipe. An example of hologram, recorded within the proposed configuration, is illustrated Fig. 3(a). It should be noticed that the diffraction patterns exhibit an hyperbolic shape. This is due to the fact that, in the micropipe, wavefront curvature radii R_ξ and R_η in both x and y directions have opposite signs [18]. As a matter of fact, a cylindrical micropipe can be viewed as an astigmatic optical system. In order to validate our theoretical approach, an hologram is simulated with the same configuration than that of experimental hologram (Fig. 3(a)). The hologram simulated using Eq. (2) is given in Fig. 3(b). As in the experimental hologram, the

#123897 - $15.00 USD Received 5 Feb 2010; revised 19 Mar 2010; accepted 22 Mar 2010; published 30 Mar 2010

diffraction pattern reveals an hyperbolic shape. Moreover, the simulated interference pattern is very similar to the experimental one, the main difference between both holograms is that there is only one object in the simulated one. In order to quantitatively validate our approach, normalized intensity profile of both holograms are calculated. To limit the contribution of noise in the experimental image, intensity profiles are averaged over 50 pixels. Obtained results are presented on Fig. 4. The normalized intensity profiles I^* of both holograms are plotted in the x-direction. Figure 4 shows a good agreement between experimental and simulated data. High-frequency fringes observable in the experimental profile are due to the fact that several particles are present in the object field, whereas only one is present in the simulated profile.

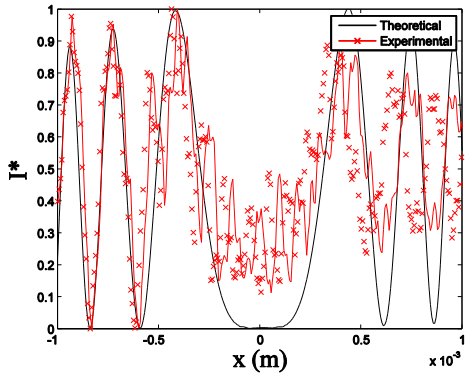

Fig. 4. Comparison of the simulated and the experimental normalized intensity profiles

We have presented a numerical approach that allow to simulate micropipe flows holograms. This approach has been qualitatively and quantitatively validated, showing the ability of our ABCD-matrices approach to deal with microchannel flows. We now intend to study a real micropipe flow. In Section 3, the mathematical definition of fractional Fourier transformation (FRFT) is recalled and applied to reconstruct images of particles moving in a micropipe flow.

3. Micropipe flow visualization

3.1. Two-dimensional fractional Fourier transformation

FRFT is a generalization of the classical Fourier transformation, which is widely used in signal processing [27]. The FRFT of order $a_x = (2\alpha_x)/\pi$ and $a_y = (2\alpha_y)/\pi$, with $0 \le |\alpha_{x,y}| \le \pi/2$, of the two-dimensional function $I(x,y)$ is given by [28–30]:

$$\mathcal{F}_{\alpha_x,\alpha_y}\left[I(x,y)\right](x_a,y_a) = \int_{\mathbb{R}^2} N_{\alpha_x}(x,x_a)\,N_{\alpha_y}(y,y_a)\,I(x,y)\,dxdy, \qquad (8)$$

with the FRFT kernel

$$N_{\alpha_p}(x,x_a) = C(\alpha_p)\exp\left(i\pi\frac{x^2+x_a^2}{s_p^2\tan\alpha_p}\right)\exp\left(-\frac{i2\pi x_a x}{s_p^2\sin\alpha_p}\right). \qquad (9)$$

Here $p = x, y$. The energy conservation, in a given fractional domain, is ensured by $C(\alpha_p)$. The parameter s_p is linked to the recording device by $s_p^2 = N_p^{px}\delta_p^2$, where N_p^{px} stand for the number of pixels in both directions and δ_p their pitch (spatial sampling rate). The equivalence between FRFT and classical Fresnel formulation has been proved by Pellat Finet

#123897 - $15.00 USD Received 5 Feb 2010; revised 19 Mar 2010; accepted 22 Mar 2010; published 30 Mar 2010

[31]. Moreover, FRFT is well suited for reconstruction of astigmatic holograms [18]. Therefore, FRFT will be chosen for our numerical treatments.

3.2. Numerical focusing: optimal fractional orders

Using FRFT to refocus over each particle image consists in compensating quadratic phases contained by the hologram (Eq. (2)) with the ones of the FRFT kernel (Eq. (9)). The quadratic phases of the hologram are given by [16]:

$$\varphi = \frac{\pi}{\lambda}\left[\left(\frac{M_x - D_2^x}{B_2^x}\right)x^2 + \left(\frac{M_y - D_2^y}{B_2^y}\right)y^2\right], \tag{10}$$

whereas, the FRFT kernel quadratic phases are derived from Eq. (9):

$$\varphi_a = \pi\left(\frac{\cot\alpha_x}{s_x^2}x^2 + \frac{\cot\alpha_y}{s_y^2}y^2\right). \tag{11}$$

Quadratic phase compensation is performed when

$$\varphi_a \pm \varphi = 0. \tag{12}$$

Optimal FRFT orders are found when condition (12) is fulfilled. Thus, their mathematical expressions are:

$$a_x = \frac{2}{\pi}\arctan\left[\mp\frac{\lambda B_2^x}{s_x^2\left(M_x - D_2^x\right)}\right],\ a_y = \frac{2}{\pi}\arctan\left[\mp\frac{\lambda B_2^y}{s_y^2\left(M_y - D_2^y\right)}\right]. \tag{13}$$

It should be noted that optimal fractional orders contain information about the whole experimental set-up: information about the recording device is contained in $s_{x,y}$, the $M_{x,y}$ terms are associated with the beam used to record holograms, and geometry of the pipe is taken into account by $B_2^{x,y}$ and $D_2^{x,y}$ (effective propagation distances are also taken into account by $B_2^{x,y}$ and $D_2^{x,y}$). Thus, a_x and a_y can be viewed as parameters that synthesize the recording-reconstruction process. Their evolutions against the δ position within the pipe permits to determine the interference pattern shape in the CCD sensor plane: fractional orders with the same signs are associated to elliptical interference fringes, whereas fractional orders exhibiting opposite signs are linked to hyperbolic shaped interference patterns. Moreover, applying to our holograms a FRFT of optimal fractional orders makes it possible to bring particles, located in the pipe, back to focus.

3.3. Application to micropipe flow visualization

The experimental set-up proposed Fig. 1 is used to record micropipe flow holograms. Here, z_p is fixed to $z_p = 11mm$, and $z_{l_1} = 3mm$. The CCD sensor shutter is set to $20\mu s$. It is, therefore possible to record hologram sequences. Here, the flow to be studied is seeded with 5µm in diameter latex beads, and illuminated with a $\lambda = 635nm$ fiber coupled laser diode.

#123897 - $15.00 USD Received 5 Feb 2010; revised 19 Mar 2010; accepted 22 Mar 2010; published 30 Mar 2010

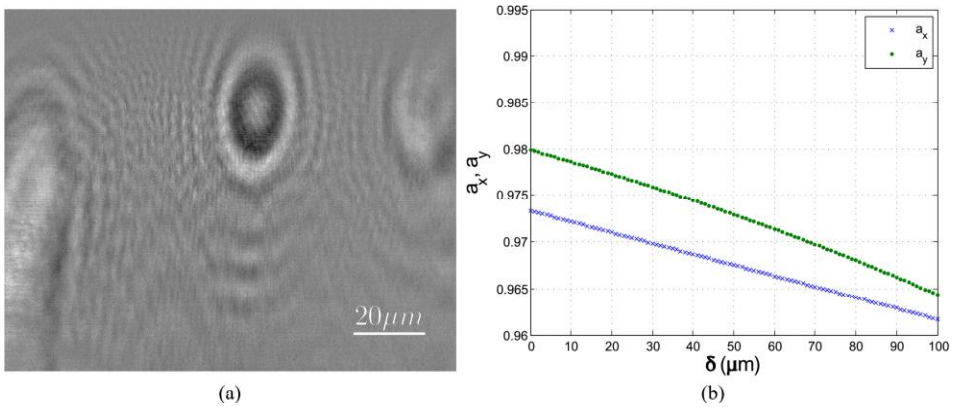

(a) (b)

Fig. 5. (a) Hologram obtained with $z_p = 11mm$ and $z_{h_1} = 3mm$. (b) Evolution of the fractional orders against observation position within the pipe.

An example of recorded hologram is proposed Fig. 5(a). It can be noticed that, under this configuration, the recorded interference pattern has an elliptic shape. This aspect is confirmed by Fig. 5(b). Here, the fractional Fourier transformation orders a_x and a_y are plotted versus the observation position in the microchannel (fractional orders a_x and a_y are estimated using Eq. (13)). Both orders have the same sign.

We now intend to use FRFT to reconstruct the hologram sequence. Using Eq. (13) allows to select a reconstruction plane within the micropipe. Then, applying FRFT to each hologram of the sequence allows to visualize particle motion comparatively to the chosen reconstruction plane.

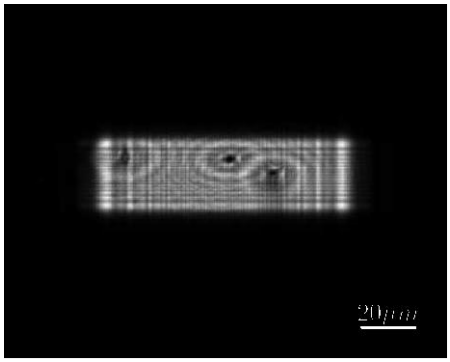

Fig. 6. (Media 1) FRFT reconstruction of the sequence of holograms proposed Fig. 5 with $a_x = 0.967, a_y = 0.972$

The movie of the reconstruction is proposed Fig. 6 (Media 1). Particle motion is almost linear. It should be noticed that some particles that are out of focus are superimposed with hyperbolic fringes, whereas some others are superimposed will elliptical ones. This result is similar to that of Ref [20]. where elliptical and hyperbolic interference fringes were recorded simultaneously. Thus, it might be possible to insulate a three-dimensional region of interest, in a micropipe flow, according to the interference pattern shapes.

In the next part, the possibility to distinguish a three-dimensional region of interest in this micropipe flow is discussed.

#123897 - $15.00 USD Received 5 Feb 2010; revised 19 Mar 2010; accepted 22 Mar 2010; published 30 Mar 2010

4. Three-dimensional region of interest extraction from a micropipe flow hologram

4.1. Experimental set-up

In order to perform the region of interest (ROI) selection, the experimental set-up proposed Fig. 7 is considered. This configuration is almost the same that of Fig. 1. However, a second microscope objective and a relay lens have been added, after the micropipe, in order to improve the visualization of interference patterns in the CCD plane. Moreover, the microscope objective is positioned very close to the micropipe ($z_{l_2} \to 0$) allowing to perform a spatial filtering of the beam.

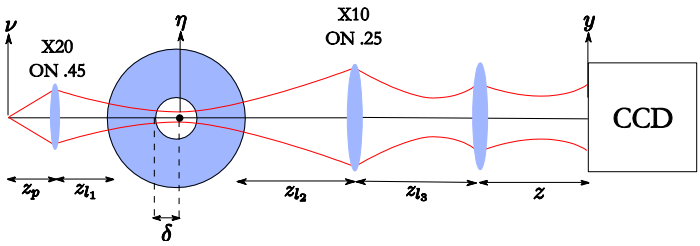

Fig. 7. 3D-ROI experimental set-up.

The relay lens is positioned at a distance $z_{l_3} = 11mm$ from the microscope objective. The propagation distance between laser source and the first microscope objective is fixed to $z_p = 20mm$. The latter is positioned $z_{l_1} = 1.5mm$ from the micropipe. Holograms are recorded on a 1624×1234 CCD sensor with a pixel pitch of $4.4\mu m$ located at the distance $z = 30mm$ from the second objective lens. In order to estimate the fractional orders, it is necessary to calculate the new ABCD matrices used to characterize the configuration proposed Fig. 7. Then, using Eqs. (4) and (7), propagation of the reference and diffracted beams are calculated. Finally, using the Eq. (13) to evaluate the evolution of the fractional orders, it is possible to determine whether a ROI is distinguishable or not.

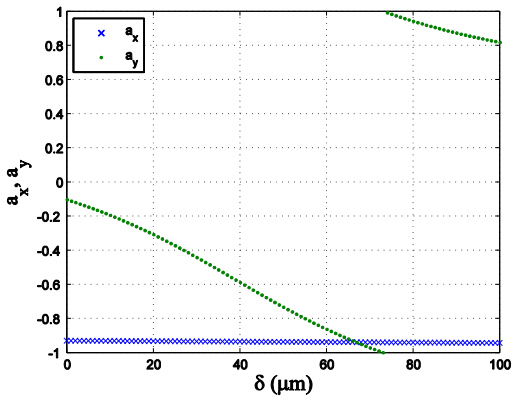

Fig. 8. Evolution of the fractional reconstruction orders in the microchannel.

A ROI is distinguishable when two different types of interference fringes are observable on the same hologram. As discussed in section 3.2, for fractional orders exhibiting the same signs, observed fringes will be elliptic, whereas fractional orders with opposite signs will be associated to hyperbolic interference patterns.

The evolution of the fractional orders in the pipe are plotted, versus the object position δ, on Fig. 8. The discontinuity of the a_y value reveals the presence of a waist in the

#123897 - $15.00 USD Received 5 Feb 2010; revised 19 Mar 2010; accepted 22 Mar 2010; published 30 Mar 2010

$y-$ direction. According to Fig. 8, two areas can be isolated: for δ ranging from $\delta = 0\mu m$ to $\delta \approx 70\mu m$, fractional orders a_x and a_y are of the same sign. Particles located in this region are supposed to generate elliptical interference fringes, whereas particles located elsewhere (*i.e.* for δ ranging from $\delta \approx 70\mu m$ to $\delta = 100\mu m$) will generate hyperbolic fringes. In other words, particles located from $\delta \approx 70\mu m$ to $\delta = 100\mu m$ will be considered to be in the ROI.

4.2. Experimental results

The possibility to select a 3D-ROI has been theoretically discussed. To confirm the presence of a ROI, an experiment has been performed using set-up parameters proposed section 4.1. Particle hologram recorded according to this configuration is presented Fig. 9(a). Here, $5\mu m$ in diameter latex beads have been used to seed the studied flow. It can be noticed that both elliptic and hyperbolic interference patterns are observed. However, only images of particles producing hyperbolic interference fringes have to be reconstructed.

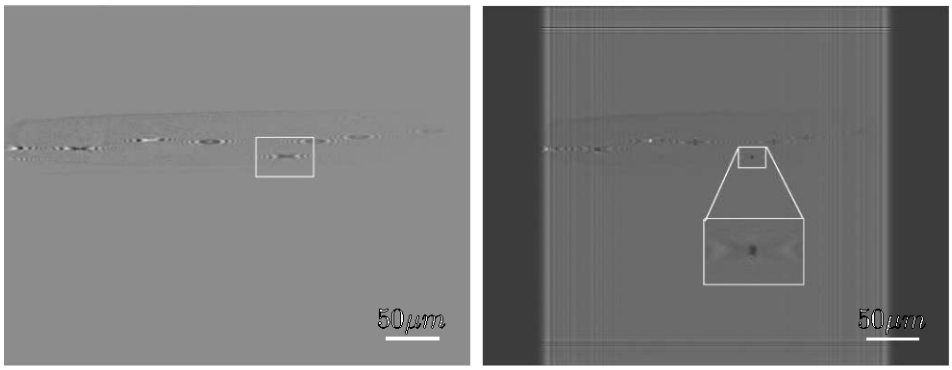

Fig. 9. (a) Hologram with a 3D-ROI. (b) FRFT reconstruction of one particle located in the ROI.

As a matter of fact, they are associated with particles located in the selected ROI. To illustrate this point, FRFT reconstruction of one particle (marked by the white selection) in the ROI is performed. As it can be noticed from Fig. 9(b), it is possible to bring back into focus a $5\mu m$ in diameter latex bead located in the ROI. Particles located elsewhere are not brought back to focus. The possibility to isolate a three-dimensional ROI has been discussed. Working within a limited zone is either a great opportunity to reduce the amount of data to be treated or by tuning the ROI position, makes it possible to refine hologram treatment in a selected zone (for instance, near the micropipe walls). Moreover, it might be regarded as a new method to enhance axial localization of objects that are contained in a micropipe flow.

4.3. Influence of the relay lens to CCD sensor distance: object axial localization improvement

The presence of a 3D-ROI has been both theoretically and experimentally proved. Here, particles to be reconstructed are selected according to their interference pattern shape. Either elliptical or hyperbolic shaped fringes can be treated independently. Several experimental parameters such as microscope objective position may influence the ROI localization. We will here investigate the influence of the relay lens to CCD sensor distance.

#123897 - $15.00 USD Received 5 Feb 2010; revised 19 Mar 2010; accepted 22 Mar 2010; published 30 Mar 2010

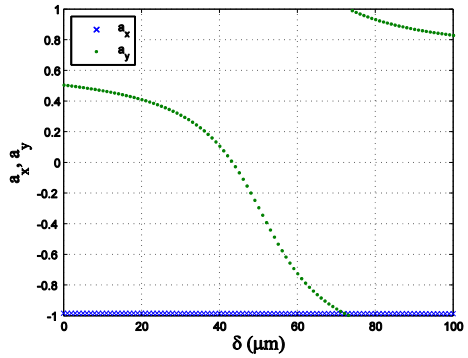

Fig. 10. Evolution of the fractional reconstruction orders in the microchannel for $z = 80mm$.

The influence of the distance z is illustrated by Fig. 10. Here, the evolution of the fractional orders is plotted versus the location of the object within the micropipe. Three areas can be distinguished from Fig. 10:

1. For δ ranging from $0\mu m$ to $45\mu m$, the interference fringes recorded will be hyperbolic.

2. For δ ranging from $70\mu m$ to $100\mu m$, interference patterns will also be hyperbolic

3. Between the above mentioned, elliptical interference patterns will be observable.

The distance z has an influence on zone 3: the higher z, the smaller the zone 3. So far, particles considered in the ROI generate hyperbolic fringes. However, as can be noticed from Fig. 10, in the zone 3, there is a rapid decrease of the fractional order values. In other words, axial particle position determination will be more sensitive to a slight variation of the fractional order values. Thus, working under this configuration is a great opportunity to enhance axial particle location accuracy. To illustrate this point, the sensitivity of the reconstruction distance to a bias in the fractional order calculation is estimated.

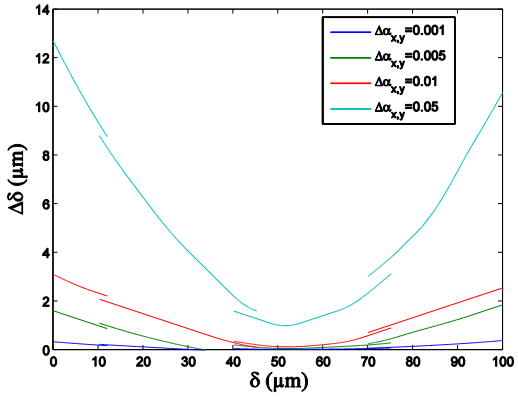

Fig. 11. Estimation of the reconstruction distance error over the microchannel for different bias in fractional order values.

Obtained results are proposed on Fig. 11. The evolution of the error in the reconstruction distance is plotted, versus the position of the object within the pipe, for bias in fractional order value ranging from 0.01 to 0.001. It should be noted that other contribution to the error in axial position estimation (such as particle diameter, signal to noise ratio of the reconstructed image …) are not taken into account. As expected by the analysis of Fig. 10, the axial position

#123897 - $15.00 USD Received 5 Feb 2010; revised 19 Mar 2010; accepted 22 Mar 2010; published 30 Mar 2010

error, that is due to a bias in the optimal order estimation, is minimal for particles located in zone 3 (*i.e.* for δ ranging from $45\mu m$ to $70\mu m$).

5. Conclusion

We have applied digital in-line holography to micropipe flow visualization. A theoretical approach, based on the ABCD matrices formalism, has been proposed and qualitatively compared with experimental holograms. Using the fractional Fourier transformation makes it possible to reconstruct holograms and to follow the particle motion. The possibility to insulate a three-dimensional region of interest in a micropipe flow has been discussed. As a matter of fact, due to the astigmatism of the reference beam, two types of interference fringes are observable: elliptic and hyperbolic fringes. Theoretical characterization of the ROI has been performed. Experimental holograms have been successfully reconstructed using fractional Fourier transformation. Finally, it has been shown that this configuration makes it possible to enhance particle axial location accuracy. The main interest of this method is that no heavy calculation processes are needed: axial localization enhancement is made possible by the experimental configuration used to record micropipe flow holograms.

6. Appendix: propagation of the beam from the particle plane to the CCD sensor plane

Propagation to the CCD sensor plane is calculated using the generalized Huygens-Fresnel integral (see Eqs. (3) and (5)).

6.1. Amplitude distribution $\mathcal{R}(x,y)$

The amplitude distribution of the reference beam $\mathcal{R}(x,y)$ is given by analytical developments of Eq. (3). Its mathematical expression is:

$$\mathcal{R}(x,y) \propto \exp\left[-\frac{\pi}{\lambda}\left(\frac{N_x}{B_2^x}x^2+\frac{N_y}{B_2^y}y^2\right)\right]\exp\left[i\frac{\pi}{\lambda}\left(\frac{M_x}{B_2^x}x^2+\frac{M_y}{B_2^y}y^2\right)\right], \qquad (14)$$

where

$$\begin{aligned} M_{x,y} &= D_2^{x,y} + \frac{\left(\frac{\pi\omega_{1_{x,y}}^2}{\lambda B_2^{x,y}}\right)^2\left(\frac{B_2^{x,y}}{R_{1_{x,y}}}-A_2^{x,y}\right)}{1+\left(\frac{\pi\omega_{1_{x,y}}^2}{\lambda B_2^{x,y}}\right)^2\left(\frac{B_2^{x,y}}{R_{1_{x,y}}}-A_2^{x,y}\right)^2}, \\ N_{x,y} &= \frac{\frac{\pi\omega_{1_{x,y}}^2}{\lambda B_2^{x,y}}}{1+\left(\frac{\pi\omega_{1_{x,y}}^2}{\lambda B_2^{x,y}}\right)^2\left(\frac{B_2^{x,y}}{R_{1_{x,y}}}-A_2^{x,y}\right)^2}. \end{aligned} \qquad (15)$$

Coefficients $M_{x,y}$ and $N_{x,y}$ contain information about both waist width $\omega_{1_{x,y}}$ and wavefront curvature radii $R_{1_{x,y}}$.

6.2. Amplitude distribution $\mathcal{O}(x,y)$

Amplitude distribution of the diffracted beam $\mathcal{O}(x,y)$, can be estimated using Eq. (5). By replacing Eq. (6) in Eq. (5), and defining:

#123897 - $15.00 USD Received 5 Feb 2010; revised 19 Mar 2010; accepted 22 Mar 2010; published 30 Mar 2010

$$\frac{1}{\omega_{1_{x_{eq}}}^2}=\frac{1}{\omega_{1_x}^2}+\frac{\Re\{B_k\}}{b^2};\quad \frac{1}{\omega_{1_{y_{eq}}}^2}=\frac{1}{\omega_{1_y}^2}+R_{ell}^2\,\frac{\Re\{B_k\}}{b^2}$$
$$\frac{1}{R_{1_{x_{eq}}}}=\frac{1}{R_{1_x}}+\frac{\Im\{B_k\}\lambda}{\pi b^2};\quad \frac{1}{R_{1_{x_{eq}}}}=\frac{1}{R_{1_x}}+R_{ell}^2\,\frac{\Im\{B_k\}\lambda}{\pi b^2}, \tag{16}$$

with $\Re$ and $\Im$ standing for real and imaginary part respectively, the analytical expression of the diffracted beam is found to be:

$$\mathcal{O}(x,y)\propto\exp\left[i\frac{\pi}{\lambda}\left(\frac{D_2^x}{B_2^x}x^2+\frac{D_2^y}{B_2^y}y^2\right)\right]\sum_{k=1}^{N}A_k K_2^{x_{eq}}K_2^{y_{eq}}$$
$$\times\exp\left[-\frac{\pi}{\lambda}\left(\frac{N_{x_{eq}}}{B_2^x}x^2+\frac{N_{y_{eq}}}{B_2^y}y^2\right)\right]\exp\left[i\frac{\pi}{\lambda}\left(\frac{M_{x_{eq}}}{B_2^x}x^2+\frac{M_{y_{eq}}}{B_2^y}y^2\right)\right], \tag{17}$$

with

$$M_{x,y_{eq}}=\frac{\left(\frac{\pi\omega_{1_{x,y_{eq}}}^2}{\lambda B_2^{x,y}}\right)^2\left(\frac{B_2^{x,y}}{R_{1_{x,y_{eq}}}}-A_2^{x,y}\right)}{1+\left(\frac{\pi\omega_{1_{x,yeq}}^2}{\lambda B_2^{x,y}}\right)^2\left(\frac{B_2^{x,y}}{R_{1_{x,y_{eq}}}}-A_2^{x,y}\right)^2},$$
$$N_{x,y_{eq}}=\frac{\frac{\pi\omega_{1_{x,yeq}}^2}{\lambda B_2^{x,y}}}{1+\left(\frac{\pi\omega_{1_{x,yeq}}^2}{\lambda B_2^{x,y}}\right)^2\left(\frac{B_2^{x,y}}{R_{1_{x,y_{eq}}}}-A_2^{x,y}\right)^2}. \tag{18}$$

#123897 - $15.00 USD Received 5 Feb 2010; revised 19 Mar 2010; accepted 22 Mar 2010; published 30 Mar 2010